micro

MDPI

Article

Spin–Valley-Resolved Electronic and Thermodynamic Responses of Monolayer MoS_2 and WSe_2 to Strain-Induced Pseudomagnetic Fields

Asmaa Yaseen and Mohammad K. Elsaid *

Physics Department, Faculty of Science, An-Najah National University, Nablus P.O. Box 7, Palestine
* Correspondence: mkelsaid@najah.edu

Abstract

The low-energy massive Dirac Hamiltonian of strained monolayer transition metal dichalcogenides (TMDs), including the effects of strain-induced pseudomagnetic fields and intrinsic spin–orbit coupling (SOC), was employed to investigate the electronic and thermodynamic properties of MoS_2 and WSe_2. The resulting pseudo-Landau-level (PLL) spectrum was obtained and used to calculate the density of states (DOS), Fermi energy, thermal average energy, and pseudomagnetic susceptibility over a wide range of pseudomagnetic fields, temperatures, and carrier concentrations. The results demonstrate that strain-induced pseudomagnetic fields generate discrete PLLs, producing pronounced structures in the DOS and characteristic field-dependent behavior in the thermodynamic quantities. The recalculated generalized pseudofield susceptibility remains positive over the investigated field range and exhibits a pronounced low-field variation followed by a progressively weaker field dependence at higher pseudomagnetic fields. Its magnitude is strongly influenced by both pseudomagnetic field and temperature, reflecting the thermodynamic response of the electronic spectrum to the strain-induced gauge field. Furthermore, the larger intrinsic SOC of WSe_2 leads to a more pronounced spin–valley splitting and distinct thermodynamic behavior compared with MoS_2. These findings demonstrate that strain-induced pseudomagnetic fields provide an effective route for tailoring the electronic, thermodynamic, and spin–valley properties of monolayer TMDs without an externally applied real magnetic field, opening new opportunities for strain-engineered quantum, spintronic, and valleytronic applications.

Keywords: transition metal dichalcogenides (TMDs); strain engineering; pseudomagnetic field; density of states; pseudomagnetic susceptibility; spin–orbit coupling

Academic Editor: Bernardo Gonçalves Almeida

Received: 1 September 2026
Revised: 28 October 2026
Accepted: 10 November 2026
Published: 12 November 2026

Copyright: © 2026 by the authors. Licensee MDPI, Basel, Switzerland. This article is an open access article distributed under the terms and conditions of the Creative Commons Attribution (CC BY) license.

1. Introduction

The isolation of graphene by mechanical exfoliation [1] opened new opportunities for exploring atomically thin materials for next-generation nanoelectronics. However, its vanishing band gap limits applications requiring efficient current switching, motivating interest in semiconducting transition metal dichalcogenides (TMDs) [2]. These layered materials combine strong in-plane bonding with weak interlayer van der Waals interactions, enabling monolayer isolation and heterostructure assembly [2,3]. Group-VI TMDs, including MoS_2 and WSe_2, exhibit thickness-dependent electronic properties; in particular, the transition from an indirect band gap in multilayer or bulk MoS_2 to a direct

band gap in the monolayer limit has been established experimentally [4,5]. Their inequivalent K and K′ valleys, valley-dependent optical selection rules, and intrinsic spin–orbit coupling (SOC) provide a platform for coupled spin–valley physics [6].

Mechanical strain provides a route for continuously tuning these properties without changing chemical composition [7]. By modifying bond lengths and orbital overlap, strain changes electronic hopping amplitudes and the low-energy band structure [8]. Experiments have demonstrated local band-gap tuning and changes in optical emission in atomically thin MoS_2 [9,10], as well as a strain-induced direct-to-indirect band-gap transition in monolayer WS_2 [11]. These observations establish the sensitivity of TMD electronic states to deformation, although conventional strain-induced band shifts should be distinguished from pseudomagnetic quantization.

Beyond conventional band-structure tuning, spatially nonuniform strain can generate effective gauge potentials and valley-contrasting pseudomagnetic fields [12]. Such fields preserve overall time-reversal symmetry and can produce pseudo-Landau levels (PLLs). In graphene nanobubbles, scanning tunneling spectroscopy revealed PLLs associated with pseudomagnetic fields exceeding 300 T [13]. Complementary measurements have resolved millitesla-scale pseudofields through quantum-oscillation imaging [14], while graphene heterostructures exhibit twist-dependent PLL spectra [15]. Transport spectroscopy has also extracted strain-induced pseudofields from beating in quantum oscillations under an applied magnetic field [16].

For monolayer TMDs, Rostami et al. [12] developed a Slater–Koster tight-binding description and an effective low-energy strain Hamiltonian, while Sahu and Satpathy [8] formulated strain-dependent Hamiltonians near the valley points. Shayeganfar [17] investigated pseudogauge-field effects on the electronic structure and anomalous valley Hall conductivity of TMD nanoribbons. Complementary calculations for graphene nanobubble superlattices linked density of states (DOS) resonances and conductance features to PLL formation [18]. Particularly relevant to the present framework, Boev et al. [19] studied impurity-band optical transitions in TMD monolayers under a strain-induced synthetic magnetic field.

Recent reviews have further highlighted advances in strain engineering and local strain control in two-dimensional semiconductors and TMDs, including methods for spatially tailoring strain fields and tuning electronic, optical, and valley-dependent responses [20–22].

These developments motivate a comparative analysis of how the established PLL spectrum governs electronic occupations and thermal responses in MoS_2 and WSe_2. Building on this theoretical foundation, the present study focuses on the interplay of pseudomagnetic field, temperature, carrier density, and SOC within a common low-energy description.

In this work, we investigate strained monolayer MoS_2 and WSe_2 within the low-energy massive Dirac framework, following the strain-induced pseudomagnetic description of Ref. [19]. We examine the conduction- and valence-band PLL spectra and their spin–valley characteristics, and calculate the density of states, Fermi energy at fixed carrier density, thermal average energy, and generalized pseudomagnetic susceptibility. Fixed-density occupations are treated using Fermi–Dirac statistics, whereas branch-resolved thermal averages are evaluated within a single-particle canonical description. The susceptibility characterizes the free-energy response to the strain-induced pseudofield, not to an independently applied real magnetic field. This comparison clarifies the electronic and thermal signatures of strain-induced quantization within the specified model.

2. Theoretical Model

2.1. Low-Energy Hamiltonian and Strain Coupling

Within the low-energy regime of group-VI monolayer TMDs, the electronic spectrum is governed by states in the vicinity of the two inequivalent valleys K and K′ at the corners of the Brillouin zone. In contrast to graphene, monolayer TMDs exhibit a finite direct band gap together with strong intrinsic SOC, predominantly originating from the transition metal d orbitals. The absence of inversion symmetry, combined with strong SOC, gives rise to a characteristic coupling between the spin and valley degrees of freedom.

Near the K and K′ valleys, the conduction-band edge is dominated primarily by the transition-metal d_{z^2} orbital, whereas the valence-band edge is mainly formed by the combinations $\left(d_{x^2-y^2} + i\eta d_{xy}\right)$ [23]. Here, $\eta = +1$ and -1 label the K and K′ valleys, respectively. The distinct orbital-angular-momentum character of these states results in markedly different SOC splittings: the valence band exhibits a pronounced spin splitting, while the conduction band retains a smaller but finite contribution. Although weaker, the conduction-band splitting becomes relevant on the meV energy scale, particularly in W-based TMDs such as WSe_2. Accordingly, both conduction and valence band SOC contributions are retained in the low energy Hamiltonian considered here.

For a fixed valley index $\eta = \pm 1$ and spin index $s = \pm 1$, we write the unstrained Hamiltonian in a form that permits intrinsic SOC in both band sectors [24],

$$H_{\eta s}^{0} = \hbar v_F\left(\eta\sigma_x p_x + \sigma_y p_y\right) + \left[\frac{\Delta}{2} + \frac{\eta s}{2}(\lambda_c - \lambda_v)\right]\sigma_z + \frac{\eta s}{2}(\lambda_c + \lambda_v)I \quad (1)$$

where Δ denotes the fundamental band-gap parameter; $v_F = \frac{at}{\hbar}$ the Fermi velocity, a the lattice constant; t is the effective hopping integral; $2\lambda_c$ and $2\lambda_v$ are the intrinsic spin–orbit spilling of the conduction and valence sectors, respectively; I is the 2 × 2 identity matrix; and σ_i are Pauli matrices acting in the two-band orbital basis. The basic material parameters used for the two group-VI TMDs considered here are listed in Table 1.

The corresponding matrix representation is

$$H_{\eta s}^{0} = \begin{pmatrix} \frac{\Delta}{2} + \eta s\lambda_c & \hbar v_F\left(\eta k_x - ik_y\right) \\ \hbar v_F\left(\eta k_x + ik_y\right) & -\frac{\Delta}{2} + \eta s\lambda_v \end{pmatrix} \quad (2)$$

The spectrum depends on the combined valley-spin index $q \equiv \eta s$, so that the time-reversal-related pairs $K\uparrow$ and $K'\downarrow$ belong to the same branch, while $K\downarrow$ and $K'\uparrow$ form the opposite branch.

Table 1. Fitting parameters for relaxed monolayer group-VI TMDs [6]. The lattice constant a is given in Å, while the effective hopping parameter t, the band gap Δ, and the SOC parameter $2\lambda_v$ and $2\lambda_c$ are expressed in eV.

Material	a	t	$2\lambda_v$	$2\lambda_c$	Δ
MoS_2	3.193	1.10	0.15	0.003	1.66
WSe_2	3.310	1.19	0.46	0.014	1.60

To describe the influence of a smooth lattice deformation on the low-energy electronic structure of a monolayer TMD, one introduces the continuum strain tensor. The in-plane displacement of a unit cell is represented by displacement field $\mathbf{u}(\mathbf{r}) = (u_x, u_y)$,

while $h(\mathbf{r})$ denotes an out-of-plane displacement. In the long-wavelength limit, the strain tensor is

$$\varepsilon_{ij} = \frac{1}{2}\left(\partial_i u_j + \partial_j u_i + \partial_i h\ \partial_j h\right), \qquad i,j = x,y. \tag{3}$$

The present model is restricted to purely in-plane deformations, so that $h = 0$. The strain tensor then contains three independent components, ε_{xx}, ε_{yy}, and ε_{xy}. According to the D_{3h} symmetry of the monolayer, these components can be decomposed into the scalar trace $\varepsilon_{xx} + \varepsilon_{yy}$, which describes local dilation or compression, and the shear doublet formed by $\varepsilon_{xx} - \varepsilon_{yy}$, and $2\varepsilon_{xy}$.

To the first order in the strain, symmetry permits two diagonal deformation-potential terms and one off-diagonal shear term in the two-band Hamiltonian [20],

$$H_\varepsilon = \beta_0 t\left(\varepsilon_{xx} + \varepsilon_{yy}\right)I + \beta_1 t\left(\varepsilon_{xx} + \varepsilon_{yy}\right)\sigma_z + \beta_2 t\left[\left(\varepsilon_{xx} - \varepsilon_{yy}\right)\sigma_x - 2\eta\varepsilon_{xy}\sigma_y\right] \tag{4}$$

The dimensionless coefficients β_0, β_1, and β_2 characterize the coupling of the low-energy electronic states to lattice deformation. The trace terms modify the local band energies, whereas the β_2 shear term has the same matrix structure as the Dirac kinetic coupling and may therefore be absorbed into a valley-dependent pseudovector potential.

The shear contribution can be incorporated into the kinetic Dirac Hamiltonian through the coupling substitution $\boldsymbol{\Pi}_{\boldsymbol{\eta}} = \mathbf{p} - e\mathbf{A}_{\boldsymbol{\eta}}$, where the valley dependent strain induced pseudovector potential is

$$e\boldsymbol{A}_\eta = \frac{\hbar\beta_2}{a}\,\eta\left(\varepsilon_{yy} - \varepsilon_{xx},\, 2\varepsilon_{xy}\right) \tag{5}$$

The corresponding strain-induced pseudomagnetic field is obtained from the curl of the pseudovector potential, $\boldsymbol{B}_\eta = \left(\nabla \times \mathbf{A}_\eta\right)_z$. Because $\mathbf{A}_\eta$ is proportional to the valley index η, the induced field reverses sign between K and K′. Therefore, strain produces a valley-contrasting magnetic field rather than an ordinary magnetic field. This sign reversal is essential: the deformation does not break time-reversal symmetry, even though carriers in each individual valley experience Landau-like orbital quantization. Thus, the strain-induced field should be regarded as a synthetic or pseudomagnetic field.

2.2. Pure-Shear Strain and Pseudomagnetic Field

A spatially uniform strain tensor gives a constant $\mathbf{A}_\eta$ and therefore zero curl. Hence, a nonzero uniform pseudomagnetic field cannot be generated by a mechanically uniform strain within this gauge-field description. Instead, the required deformation must be spatially nonuniform, with strain components whose first spatial derivatives are constant. A standard triaxial-like pure-shear profile satisfying this requirement is

$$u_x = -Cxy, \qquad u_y = \frac{C}{2}\left(y^2 - x^2\right) \tag{6}$$

where C has dimensions of inverse length and controls the strain gradient. Substitution of Equation (6) into Equation (3) gives

$$\varepsilon_{xx} = \frac{\partial u_x}{\partial x} = -Cy, \qquad \varepsilon_{yy} = \frac{\partial u_y}{\partial y} = Cy, \qquad \varepsilon_{xy} = \frac{1}{2}\left(\frac{\partial u_x}{\partial y} + \frac{\partial u_y}{\partial x}\right) = -Cx \tag{7}$$

The trace of the strain tensor therefore vanishes, $\varepsilon_{xx} + \varepsilon_{yy} = 0$; accordingly, the leading hydrostatic scalar terms proportional to β_0 and β_1 vanish for this ideal pure-shear configuration. The remaining deformation acts through the gauge term. Substitution of the strain components into the vector potential gives $\mathbf{A}_\eta = \eta\frac{2\hbar\beta_2 C}{ea}(y, -x)$; this pseudovector potential has the form of a symmetric gauge and therefore produces a

spatially uniform perpendicular pseudomagnetic field. Taking the curl gives $\boldsymbol{B}_\eta = -\eta B_s$, where the positive field magnitude B_s is $B_s = \frac{4\hbar\beta_2 C}{ea}$. Hence, the two time-reversed valleys experience pseudomagnetic fields of equal magnitude and opposite sign. The mechanical deformation required to generate a prescribed field is therefore determined by $C = \frac{ea}{4\hbar\beta_2} B_s$. These relations provide the direct connection between the real-space strain profile and the pseudomagnetic field used in the electronic calculations.

Since the strain components ε_{xx}, ε_{yy}, and ε_{xy} vary linearly with Cx or Cy, the characteristic strain amplitude over a region of linear size L scales is $\varepsilon_{char} \simeq CL = \frac{eaB_sL}{4\hbar\beta_2}$. The local small-strain continuum description therefore requires $CL \ll 1$. At a fixed admissible strain amplitude, increasing B_s requires a larger strain gradient and consequently reduces the spatial region over which the continuum pure-shear description can remain mechanically moderate. The numerical conversion between B_s and C is material-dependent through both the lattice constant a and the shear-strain coupling β_2.

For MoS_2, using $a = 3.193$ Å and the commonly used value $\beta_2 = 3$ [19], the SI relation above gives $C \simeq 0.40\ \mu m^{-1}$ for $B_s = 10$ T, consistent with the approximate value $C \simeq 0.43\ \mu m^{-1}$ quoted in the source model of Boev et al. [19]. Requiring a characteristic local strain not larger than about 5% gives $L \lesssim 124$ nm at 10 T. At 80 T, the same estimate gives $C \simeq 3.23\ \mu m^{-1}$ and $L \lesssim 15$ nm. Accordingly, the largest pseudofields considered in the model should be interpreted as local nanoscale or idealized continuum fields rather than fields that remain uniform over an entire micron-scale flake.

For the pure-shear profile introduced above, the scalar terms vanish at first order, and the remaining strain contribution can be written as

$$H_{\text{strain}} = 2\beta_2 tCr\left(-\sin\phi\ \sigma_x + \eta\cos\phi\ \sigma_y\right) \tag{8}$$

Here, $x = r\cos\phi$ and $y = r\sin\phi$. It is convenient to introduce $b \equiv \frac{2\beta_2 C}{a} = \frac{eB_s}{2\hbar}$. Using $\hbar v_F = at$, the strain contribution then takes the compact form,

$$H_{\text{strain}} = \hbar v_F br\left(-\sin\phi\ \sigma_x + \eta\cos\phi\ \sigma_y\right) \tag{9}$$

This is the form used below to derive the PLL spectrum.

2.3. Pseudo-Landau-Level Spectrum

The complete band Hamiltonian is

$$H_{\eta s} = H^0_{\eta s} + H_{\text{strain}} \tag{10}$$

Because the resulting Hamiltonian in the symmetric gauge has cylindrical symmetry, the eigenstate can be written as the two component spinor

$$\Psi_{\eta s}(r,\phi) = \frac{1}{\sqrt{2\pi}}\begin{pmatrix} e^{i\eta(l-1)\phi}\,\psi_1(r) \\ i\eta\, e^{i\eta l\phi}\,\psi_2(r) \end{pmatrix}, \qquad l = 0, \pm1, \pm2, \ldots \tag{11}$$

The integer l follows from the single-valuedness of the wavefunction under $\phi \to \phi + 2\pi$. The two components in Equation (11) are orbital components of the two-band spinor; the real-spin degree of freedom is already represented by s.

Substituting Equation (11) into the stationary Dirac equation $H_{\eta s}\Psi_{\eta s} = E\Psi_{\eta s}$ gives the coupled radial system,

$$\left(E - \frac{\Delta}{2} - q\lambda_c\right)\psi_1 - \hbar v_F\left(\frac{d}{dr} + \frac{l}{r} + br\right)\psi_2 = 0 \tag{12}$$

$$\hbar v_F\left(\frac{d}{dr} - \frac{l-1}{r} - br\right)\psi_1 + \left(E + \frac{\Delta}{2} - q\lambda_v\right)\psi_2 = 0 \tag{13}$$

From Equation (12), $\psi_1 = \frac{\hbar v_F}{E-\Delta/2-q\lambda_c}\left(\frac{d}{dr}+\frac{l}{r}+br\right)\psi_2$. Substitution into Equation (13) eliminates ψ_1 and gives a second-order equation for the lower spinor component,

$$\frac{d^2\psi_2}{dr^2}+\frac{1}{r}\frac{d\psi_2}{dr}+\left[\frac{\left(E-E_c^{(0)}\right)\left(E-E_v^{(0)}\right)}{(\hbar v_F)^2}+2b(1-l)-\frac{l^2}{r^2}-b^2r^2\right]\psi_2=0 \quad (14)$$

Here, $E_c^{(0)}(q)=\Delta/2+q\lambda_c$ and $E_v^{(0)}(q)=-\Delta/2+q\lambda_v$ denote the corresponding spin and valley resolved band edge energies.

Introducing the dimensionless radial coordinate $\xi = br^2$ transforms Equation (14) into a dimensionless radial equation. Regularity at the origin selects the nondivergent radial behavior, whereas normalizability at a large radius requires exponential decay. These conditions motivate the substitution $\psi_2(\xi)=A_2e^{-\xi/2}\xi^{|l|/2}f(\xi)$.

Substitution into Equation (13) gives

$$\xi f''+(|l|+1-\xi)f'+\left[\frac{\left(E-E_c^{(0)}\right)\left(E-E_v^{(0)}\right)}{4b(\hbar v_F)^2}-\frac{l+|l|}{2}\right]f=0 \quad (15)$$

Equation (15) has the standard form of the associated Laguerre differential equation, which is the polynomial sector of the confluent hypergeometric equation, $\xi y''+(\alpha+1-\xi)y'+n_2y=0$. Comparing the two equations gives $\alpha=|l|$ and $n_2=\frac{\left(E-E_c^{(0)}\right)\left(E-E_v^{(0)}\right)}{4b(\hbar v_F)^2}-\frac{l+|l|}{2}$. Normalizability requires the confluent-hypergeometric series to terminate; hence $n_2=0,1,2,\ldots$. The regular solution is therefore $f(\xi)=L_{n_2}^{|l|}(\xi)$, where $L_n^{\alpha}(\xi)$ denotes an associated Laguerre polynomial. The lower radial component can thus be written as $\psi_2(r)=A_2e^{-\xi/2}\xi^{|l|/2}L_{n_2}^{|l|}(\xi)$.

Defining the PLL index by $n_2=n-\frac{l+|l|}{2}$ and combining this relation with the preceding expression for the polynomial degree gives the quantization condition

$$\left(E-E_c^{(0)}\right)\left(E-E_v^{(0)}\right)=4(\hbar v_F)^2bn \quad (16)$$

Solving the quadratic equation gives the expressions for the electron energy in conduction (c) and valence (v) bands,

$$E_{n,\eta,s}^{c,v}=\frac{q(\lambda_c+\lambda_v)}{2}\pm\frac{1}{2}\sqrt{[\Delta+q(\lambda_c-\lambda_v)]^2+8e\hbar v_F^2|B_s|\,n} \quad (17)$$

The upper sign in Equation (17) corresponds to the conduction band and the lower sign to the valence band. The upper radial component follows from the first-order system and can be expressed as $\psi_1(r)=A_1e^{-\xi/2}\xi^{|l-1|/2}L_{n_1}^{|l-1|}(\xi)$. With $n_1=n-1-\frac{l-1+|l-1|}{2}$. Together with the lower component above, these relations determine the relative amplitude A_1/A_2 and the normalized spinor wavefunction.

The angular quantum number l may be positive, negative, or zero because single-valuedness of Equation (11) requires only $l\in\mathbb{Z}$. By contrast, the Laguerre indices n_1 and n_2 are polynomial degrees and must be non-negative integers. The absolute-value factors therefore separate the allowed states into two cases.

For $l>0$, one has $|l|=l$ and $|l-1|=l-1$. Hence, $n_1=n_2=n-l, n\geq l$, with $n\geq l$ following from the requirement $n_1,n_2\geq 0$. For $l\leq 0$, including $l=0$, the absolute values instead give $|l|=-l$ and $|l-1|=1-l$. Thus, for $n\geq 1$, $n_1=n-1, n_2=n$, so both spinor components are present.

The case $n=0$ is special. The relation for $n_1=n-1-\frac{l-1+|l-1|}{2}$ then gives $n_1=-1$, which is not an admissible Laguerre-polynomial degree. Normalizability therefore requires $\psi_1=0$, and the remaining first-order equation fixes the energy to the valence-band edge,

$$E_{0,\eta,s} = E_v^{(0)}(q) = -\frac{\Delta}{2} + q\lambda_v \tag{18}$$

Thus, for the strain convention adopted here, the zeroth PLL belongs only to the valence band. The physically allowed pseudo-Landau indices are consequently

$$n_c = 1,2,3,\ldots, \qquad n_v = 0,1,2,3,\ldots \tag{19}$$

The formal positive-energy root obtained by setting $n = 0$ in Equation (17) is not an admissible conduction-band eigenstate because it does not satisfy the normalizable two-component spinor solution. The angular quantum number l labels the orbital degeneracy within each PLL, whereas the energy depends on n, η, and s.

2.4. Electronic Properties of the System

The PLL spectrum obtained above provides the basis for evaluating the electronic properties of the strained TMD monolayer. DOS specifies the number of available electronic states per unit energy and unit area. For a 2D system, each PLL carries the usual orbital degeneracy per unit area. The corresponding pseudomagnetic length is determined by the magnitude of the strain-induced field. Consistently with the allowed indices derived in Section 2.3, the conduction-band sum starts from $n = 1$, whereas the valence-band sum starts from $n = 0$. The ideal DOS is

$$D(E) = \frac{1}{2\pi l_c^2}\sum_{\mathrm{n,s},\eta} \delta(E - E_{\mathrm{n,s},\eta}) \tag{20}$$

This shows a sequence of delta functions in energy. This description is valid to an ideal, impurity-free system. In a more realistic model, however, the presence of imperfections and disorder leads to a finite broadening of the PLLs.

Therefore, the delta function which appears in the DOS expression can be replaced by a more practical expression via a Gaussian distribution with broadening parameter Γ as

$$D(E) = D_0 \sum_{\mathrm{n,s},\eta} \exp[-\frac{(E-E_{\mathrm{n,s},\eta})^2}{2\Gamma^2}] \tag{21}$$

The normalization constant is given by $D_0 = \frac{1}{2\pi l_c^2 \Gamma\sqrt{2\pi}}$, where $l_c = \sqrt{\hbar/eB_s}$ is the pseudo-magnetic length scale and Γ represents the level-broadening width. The stability of the calculated observables is checked by varying both the broadening and the cutoff. We next examine the behavior of the Fermi level with the pseudomagnetic field for a fixed carrier density. To determine the Fermi energy E_F in the presence of a pseudomagnetic magnetic field, we begin with the expression for carrier density n_e

$$n_e = \int_{-\infty}^{+\infty} D(E) f(E) dE \tag{22}$$

where $D(E)$ is the DOS given by Equation (19).

$f(E) = [\exp\{\frac{(E-E_F)}{k_B T}\} + 1]^{-1}$ is the Fermi–Dirac distribution function. Here, E_F denotes the equilibrium chemical potential μ at finite temperature and is referred to as the Fermi energy throughout this work, consistent with the very-low-temperature regime considered.

Substituting the DOS expression into Equation (22) and applying the properties of the Dirac delta function this transforms the integral into a summation over the PLLs, yielding the self-consistent equation

$$\pi n_e l_c^2 = \sum_{n,\mathrm{s},\eta} f(E_{\mathrm{n,s},\eta}) \tag{23}$$

Equation (23) is solved numerically for each value of the pseudomagnetic field B_s to obtain the variation of E_F while maintaining a fixed carrier density.

2.5. Thermodynamic and Pseudomagnetic Properties of the System

One of the primary objectives of this study is the determination of the average energy, which is a fundamental quantity to describe the thermal population of the quantized levels and to evaluate the effect of external parameters such as temperature and pseudomagnetic field B_s. The average energy $\langle E \rangle$ is evaluated within the framework of equilibrium statistical mechanics using the canonical ensemble. It is given by the following standard expression:

$$\langle E \rangle = \frac{1}{Z}\sum_{n,s,\eta} E_{\mathrm{n,s,\eta}} \exp(-\frac{E_n}{k_B T}) \tag{24}$$

where $Z = \sum_{n,s,\eta} \exp(-\frac{E_{n,s,\eta}}{k_B T})$ is the standard statistical partition function; $E_{n,s,\eta}$ denotes the discrete energy eigenvalues of the system; T is the temperature; and k_B is the Boltzmann constant.

For the valence band, the thermal average is evaluated using positive excitation energies measured from the corresponding band edge,

$$\varepsilon^{v}_{n,s,\eta}(B_s) = E^{v}_{0,s,\eta}(B_s) - E^{v}_{n,s,\eta}(B_s) \geq 0, \;\; n \geq 0. \tag{25}$$

The band-edge state thus has zero excitation energy. These energies replace the negative valence-band eigenenergies in the partition function and thermal average in Equation (24), suppressing the contribution of deeper states and yielding a convergent average as the number of retained levels is increased.

The thermodynamic response of the system to the strain-induced pseudomagnetic field is characterized through the curvature of the Helmholtz free energy with respect to B_s. Since the pseudomagnetic field originates from lattice deformation and acts with opposite signs in the two valleys, it does not represent an externally applied real magnetic field and preserves time-reversal symmetry. We therefore define the generalized pseudofield susceptibility as

$$\chi_s = -\frac{\partial^2 F}{\partial {B_s}^2} = k_B T \frac{\partial^2 \ln Z}{\partial {B_s}^2} \tag{26}$$

where $F = -k_B T \ln Z$ is the Helmholtz free energy. The quantity χ_s thus describes the thermodynamic response of the electronic system to variations of the strain-induced pseudomagnetic field.

3. Results and Discussion

This section analyzes the response of monolayer MoS_2 and WSe_2 to temperature variations and different strengths of the strain-induced pseudomagnetic field B_s. The energy spectrum, DOS, Fermi energy, average energy, and pseudofield response are the main quantities considered in this analysis. These quantities provide important information about the behavior of the monolayers under different thermodynamic and strain conditions.

First, we present the PLL spectrum obtained from the theoretical model for monolayer MoS_2 and WSe_2 as a function of the strain-induced pseudomagnetic field B_s, as shown in Figures 1 and 2. Panels (a) and (b) show the conduction- and valence-band levels, respectively. For both materials, the strain-induced pseudomagnetic field produces a discrete ladder of PLLs, with the level separation between the levels becoming more pronounced as B_s increases. This quantization arises purely from strain and does not require an externally applied real magnetic field. The states in the K valley with spin up (down) coincide with the corresponding states in the K' valley with spin down (up). This is a direct consequence of time-reversal symmetry: because the strain-induced pseudomagnetic field has opposite signs in the two inequivalent valleys, the

corresponding time-reversed spin–valley pairs remain degenerate. This behavior differs from that produced by a real magnetic field, which breaks time-reversal symmetry.

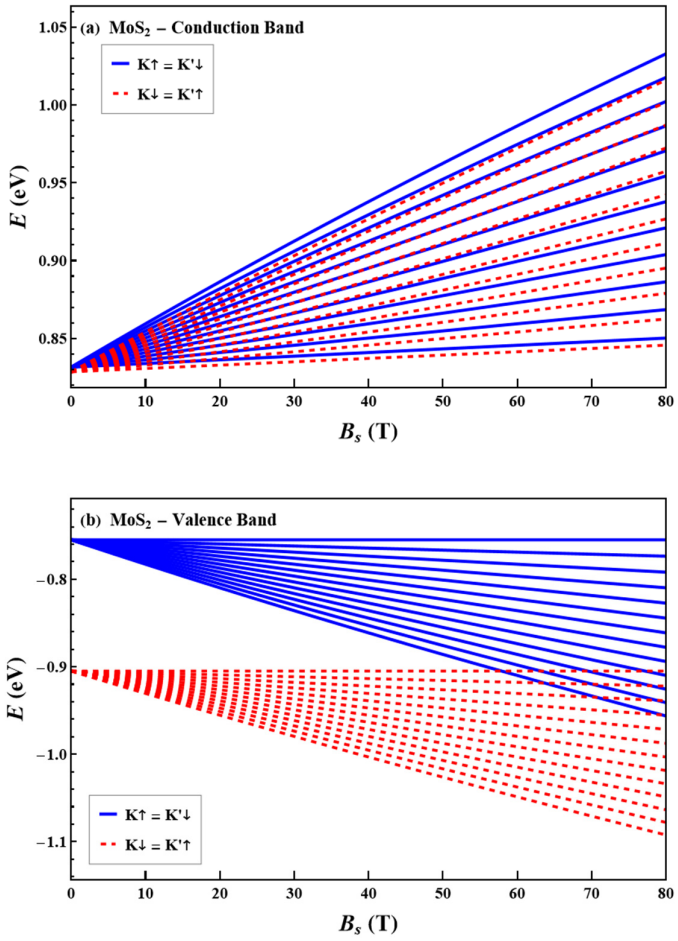


Figure 1. Pseudo-Landau levels (PLLs) of monolayer MoS_2 are plotted as a function of the strain-induced pseudomagnetic field B_s. The upper and lower panels display the conduction and valence band spectra, respectively. The two sets of curves correspond to the spin–valley configurations $K\uparrow = K'\downarrow$ (solid blue) and $K\downarrow = K'\uparrow$ (dashed red).

The behavior of the valence-band levels differs from that of the conduction band. While the conduction-band energies increase with increasing B_s, the valence-band energies decrease. Thus, the pseudomagnetic field shifts the two sets of levels in opposite directions while preserving their overall ordering. Comparing MoS_2 and WSe_2 shows clear quantitative differences in the PLL spacing and distribution, arising from their different band parameters and the stronger SOC in WSe_2. In contrast, the two opposite spin–valley branches have different SOC-induced energy offsets and different effective gaps. Their field-dependent shifts can therefore lead to crossings between PLLs belonging to different branches. These crossings are allowed within the present model because the two branches belong to distinct spin–valley sectors and no intervalley or spin–mixing interaction is included that would hybridize them and produce an avoided crossing. The stronger intrinsic SOC of WSe_2 produces a pronounced separation between the two valence-band branches, as clearly seen in Figure 2b. The conduction-band splitting is much smaller but remains relevant on the low-energy scale. Overall, the strain-induced pseudomagnetic

field provides a continuous means of tuning both the PLL spacing and the relative positions of the spin–valley-resolved states without applying a real magnetic field.

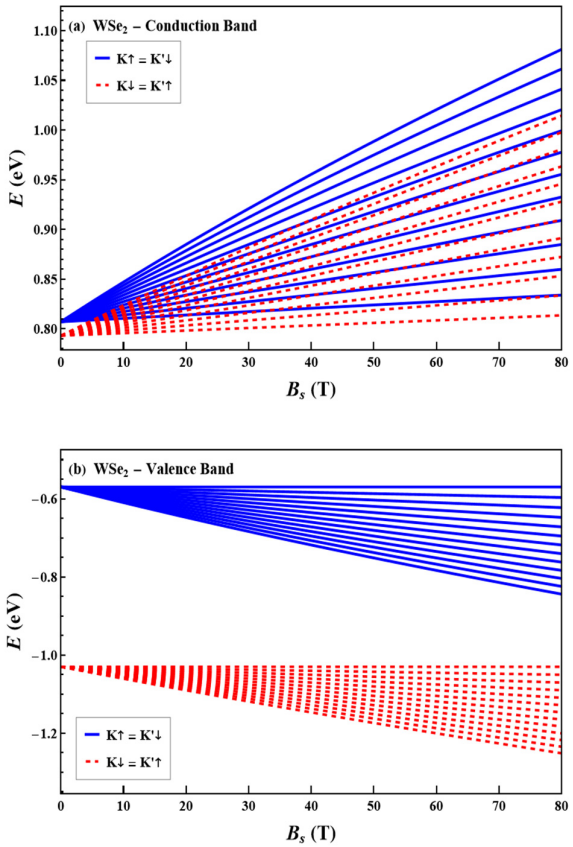


Figure 2. Pseudo-Landau levels (PLLs) of monolayer WSe_2 are plotted as a function of the strain-induced pseudomagnetic field B_s. The upper and lower panels display the conduction and valence band spectra, respectively. The two sets of curves correspond to the spin–valley configurations $K\uparrow = K'\downarrow$ (solid blue) and $K\downarrow = K'\uparrow$ (dashed red).

In Figure 3, we present the dependence of the spin-splitting energy in the conduction and valence bands of monolayer MoS_2 on the pseudomagnetic field B_s for several values of the PLL index n. We first focus on Figure 3a, where the conduction-band splitting energy increases approximately linearly with B_s. We can see that this energy separation depends not only on B_s but also on the PLL n. Specifically, higher PLLs exhibit a more pronounced variation in energy separation with increasing B_s. For example, the $n = 10$ level shows the steepest variation, whereas the $n = 1$ level changes only slightly over the same field range. The splitting energies at the K and K′ valleys behave oppositely as B_s increases in the conduction band: the splitting increases at the K valley (Figure 3a), whereas it becomes increasingly negative at the K′ valley (Figure 3c), reflecting the valley-contrasting character of the pseudomagnetic field. For the valence band, shown in Figure 3b,d, the magnitude of the splitting is relatively large at $B_s = 0$, approximately 0.150 eV for MoS_2. At the K valley, the positive splitting decreases with increasing B_s, whereas at the K′ valley, the negative splitting increases toward zero, with the variation becoming more pronounced for higher n. Comparing MoS_2 (Figure 3) with WSe_2 (Figure 4), we find that both materials exhibit the same qualitative field dependence, while the magnitude of the splitting and its field variation depend on the PLL index and the material parameters. In particular, the zero-field valence-band spin splitting is substantially larger

in WSe_2, approximately 0.460 eV, than in MoS_2, approximately 0.150 eV, owing to the stronger intrinsic SOC in WSe_2.

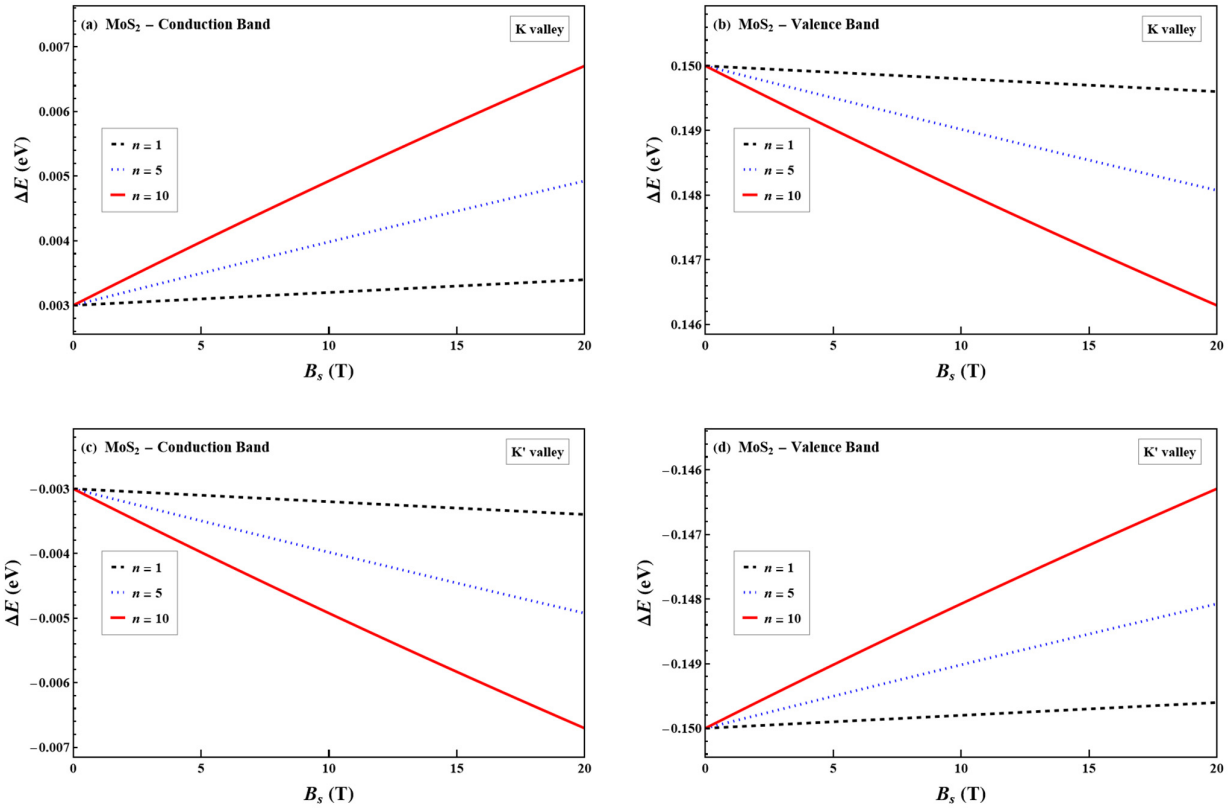


Figure 3. Dependence of the spin-splitting energy on the pseudomagnetic field B_S for different PLL indices n in monolayer MoS_2: (**a**) conduction band at the K valley, (**b**) valence band at the K valley, (**c**) conduction band at the K′ valley, and (**d**) valence band at the K′ valley.

Figure 5 illustrates how the strain-induced pseudomagnetic field modifies the normalized DOS in the valence and conduction bands of monolayer MoS_2 and WSe_2. For the adopted pure-shear strain profile, increasing B_s from 30 to 50 T corresponds to increasing the magnitude of the strain-gradient parameter. Within each spin–valley branch, the stronger pseudomagnetic field increases the energy separation between successive PLLs. At a fixed level index, the conduction-band levels shift toward higher energies, whereas the $n \geq 1$ valence-band levels shift toward lower energies. These changes modify the positions and distribution of the DOS resonances, although resonances from different branches may remain closely spaced or overlap. Differences between MoS_2 and WSe_2 reflect their distinct band parameters and intrinsic spin–orbit coupling strengths.

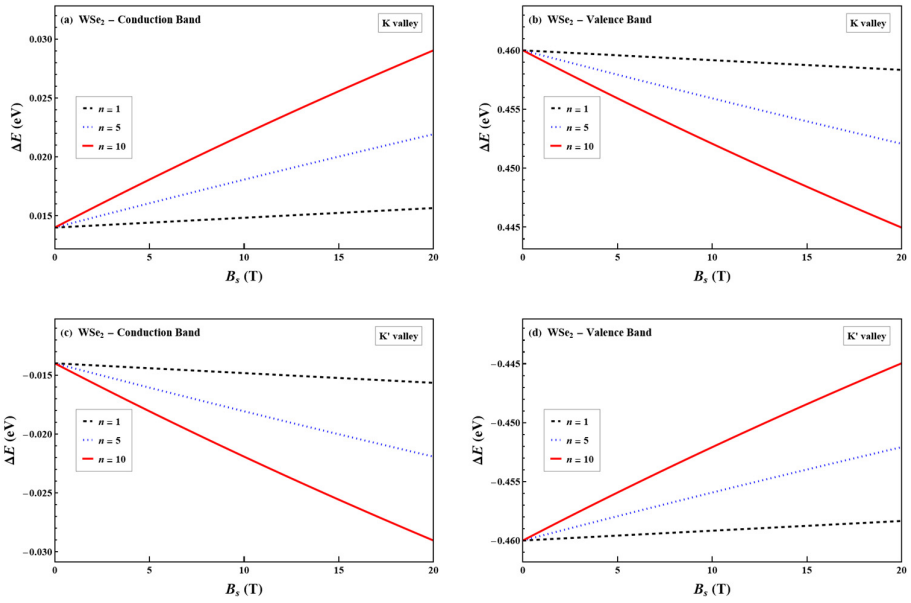


Figure 4. Dependence of the spin-splitting energy on the pseudomagnetic field B_s for different PLL indices n in monolayer WSe_2: (**a**) conduction band at the K valley, (**b**) valence band at the K valley, (**c**) conduction band at the K′ valley, and (**d**) valence band at the K′ valley.

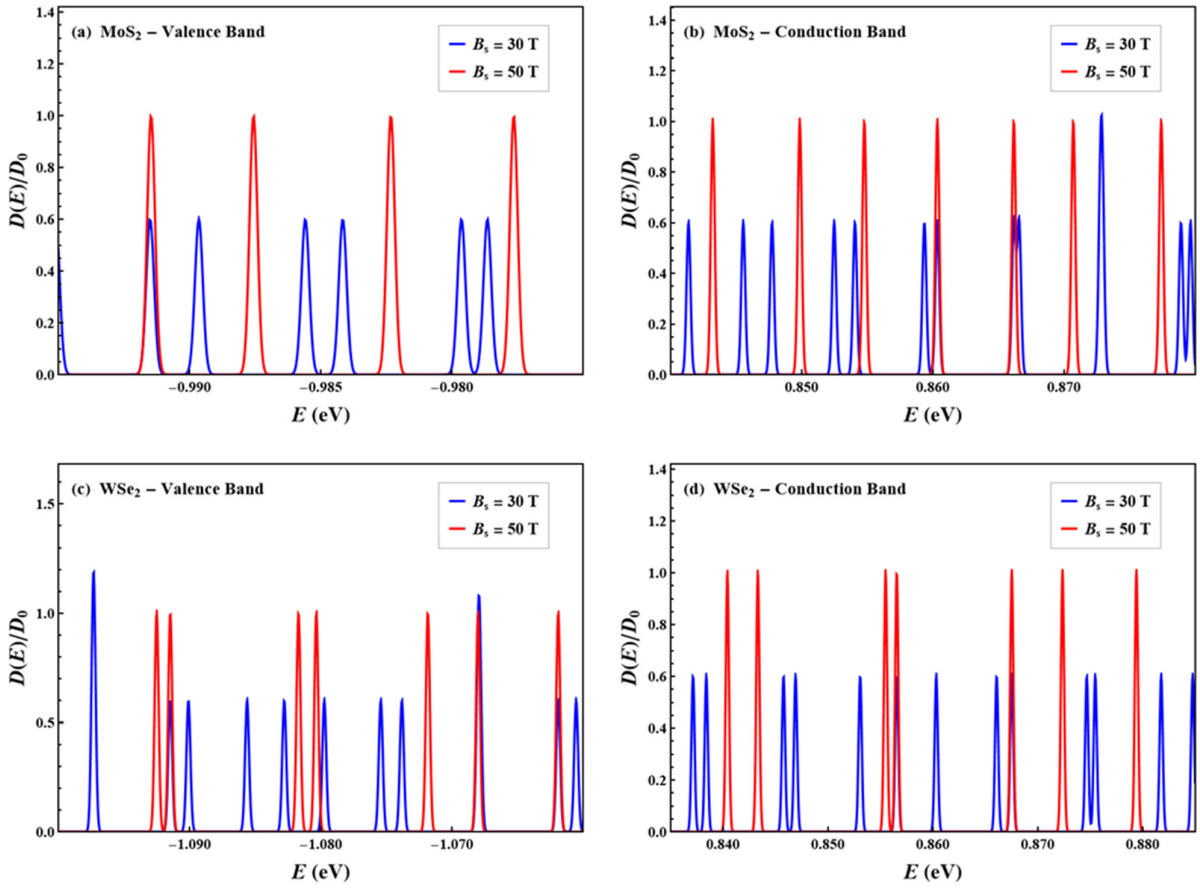


Figure 5. Normalized density of states, $D(E)/D_0$, as a function of energy for monolayer MoS_2 and WSe_2 at strain-induced pseudomagnetic fields $B_s = 30$ and 50 T. Panels (**a**,**b**) show the valence-

and conduction-band results for MoS_2, respectively, while panels (**c**,**d**) show the corresponding results for WSe_2. Blue and red curves correspond to $B_s = 30$ and 50 T, respectively. A Gaussian broadening parameter of $\Gamma = 0.15$ meV is used.

The experimental relevance of these results is a qualitative connection between strain and the electronic spectrum. Levy et al. [13] observed strain-induced pseudo-Landau quantization through tunneling spectroscopy of graphene nanobubbles, demonstrating that electronic levels generated by a strain-induced pseudomagnetic field can be resolved spectroscopically. This provides an experimental precedent for the quantization mechanism considered here, although the material and electronic spectrum differ from those of monolayer TMDs.

In monolayer MoS_2, Pető et al. [25] reported strain-dependent changes in the electronic gap and Fermi-level position using tunneling spectroscopy, complemented by photoluminescence measurements. Their measurements demonstrate that strain can measurably modify the electronic spectrum of MoS_2. However, their study concerns biaxially strained nanobubbles and does not establish the orbital PLL spectrum considered here. The qualitative connection is therefore the strain tunability of the electronic structure, rather than agreement in the direction or magnitude of individual PLL peak shifts. In the present model, this tunability is mediated by the strain-induced pseudomagnetic field. The predicted changes in resonance energies and level spacings provide specific signatures for spatially resolved tunneling spectroscopy in suitably strained TMD monolayers, provided that spectral broadening and instrumental resolution permit individual levels to be resolved.

To clarify the spin–valley contributions underlying the total DOS shown in Figure 5, Figure 6 presents the branch-resolved normalized DOS, for monolayer MoS_2 and WSe_2 at $B_s = 50$ T. The two contributions correspond to the K↑ = K′↓ and K↓ = K′↑ sectors, each containing a pair of time-reversal-related states. The relative displacement of their PLL resonances reflects the spin–valley dependence of the electronic spectrum. In the valence band, the separation between the two sets of displayed resonances is more pronounced in WSe_2 than in MoS_2, consistent with the stronger intrinsic valence-band SOC of WSe_2. In the conduction band, the two spectral sequences occupy largely overlapping energy ranges, with their relative peak positions determined by the conduction-band SOC and the PLL spectrum. Thus, Figure 6 complements the field-dependent total DOS in Figure 5 by identifying the contributions of the individual spin–valley sectors to the overall spectral response.

To further investigate the electronic structure, we plot the normalized DOS evaluated at a fixed Fermi energy, $D(E_F)/D_0$, as a function of the inverse of the strain-induced pseudomagnetic field, B_s^{-1}, for monolayer MoS_2 and WSe_2 in Figures 7 and 8, respectively. The oscillatory structure directly reflects the discrete PLL spectrum. As B_s varies, successive PLLs are brought into resonance with the selected Fermi energy, producing maxima in the DOS whenever $E = E_F$. Between successive crossings, the DOS is strongly suppressed. Since the field-dependent contribution to the PLL spectrum is governed approximately by the product nB_s, the fixed-energy crossing condition produces an approximately periodic sequence of resonances when the results are represented as a function of B_s^{-1}. The resulting DOS oscillations are therefore analogous to the inverse-field periodic quantum oscillations associated with Landau quantization and Shubnikov–de Haas-type behavior.

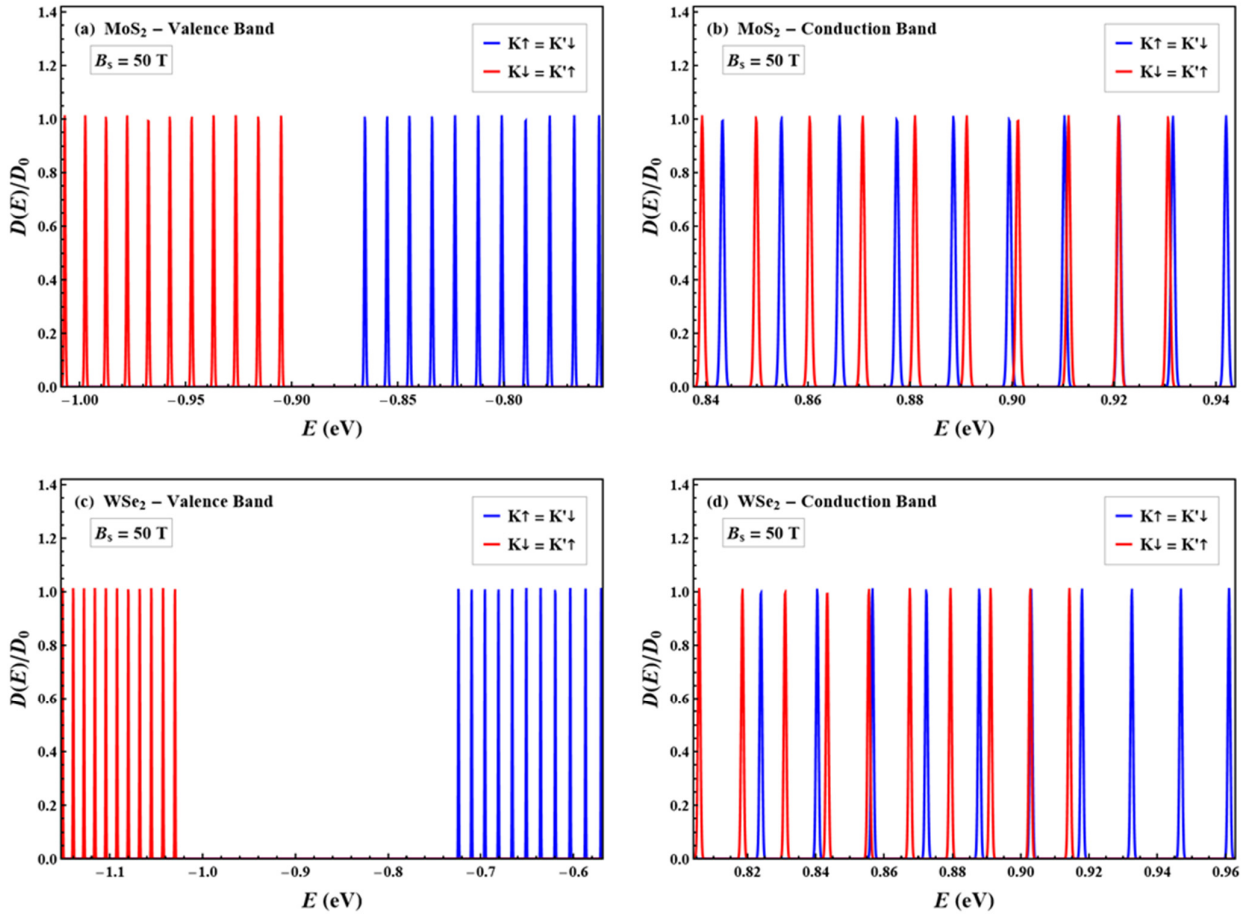


Figure 6. Branch-resolved normalized density of states, $D(E)/D_0$, as a function of energy for monolayer MoS_2 and WSe_2 at a strain-induced pseudomagnetic field $B_s = 50$ T. Panels (**a**,**b**) show the valence- and conduction-band results for MoS_2, respectively, while panels (**c**,**d**) show the corresponding valence- and conduction-band results for WSe_2. The blue and red curves correspond to the K↑ = K′↓ and K↓ = K′↑ spin–valley sectors, respectively. A Gaussian broadening parameter of $\Gamma = 0.3$ meV is used.

For MoS_2, panels (a) and (b) are evaluated at $E_F = 0.8304$ eV over different pseudomagnetic-field ranges. In the lower-field regime, a larger number of higher-index PLLs successively cross the Fermi energy, giving rise to a denser sequence of oscillations. At relatively higher pseudomagnetic fields, the separation between neighboring PLLs increases, and the individual resonances become more clearly resolved. Panel (c), evaluated at $E_F = 0.8322$ eV, demonstrates the sensitivity of the oscillatory structure to the position of the Fermi energy. Changing E_F modifies the PLL indices satisfying the resonance condition and therefore shifts the positions and spacing of the DOS maxima.

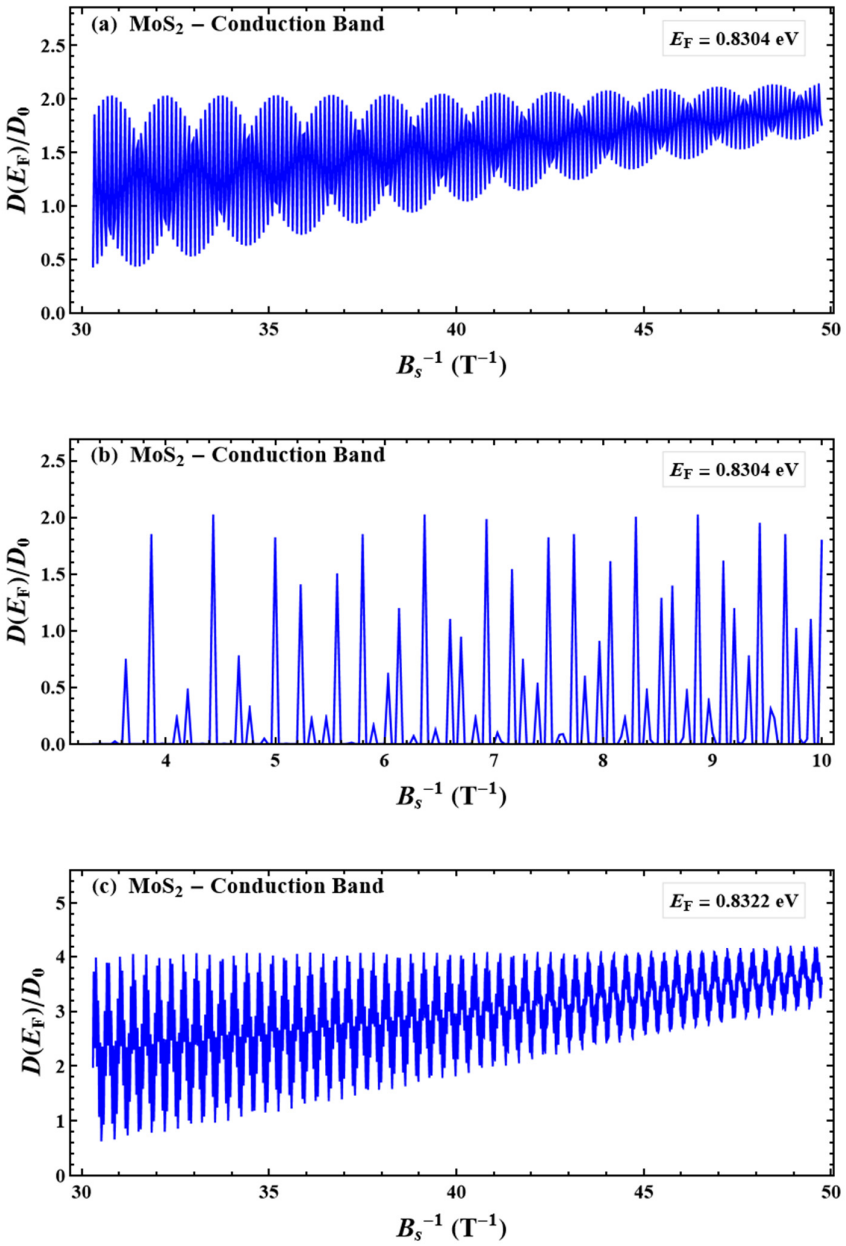


Figure 7. Normalized density of states, $D(E_F)/D_0$, as a function of the inverse of the strain-induced pseudomagnetic field, B_s^{-1}, for monolayer MoS_2. Panels (**a**,**b**) are evaluated at $E_F = 0.8304$ eV over low- and relatively higher-pseudomagnetic-field ranges, respectively, while panel (**c**) is evaluated at $E_F = 0.8322$ eV in the low-field regime. A Gaussian broadening parameter of $\Gamma = 0.0017$ meV is used.

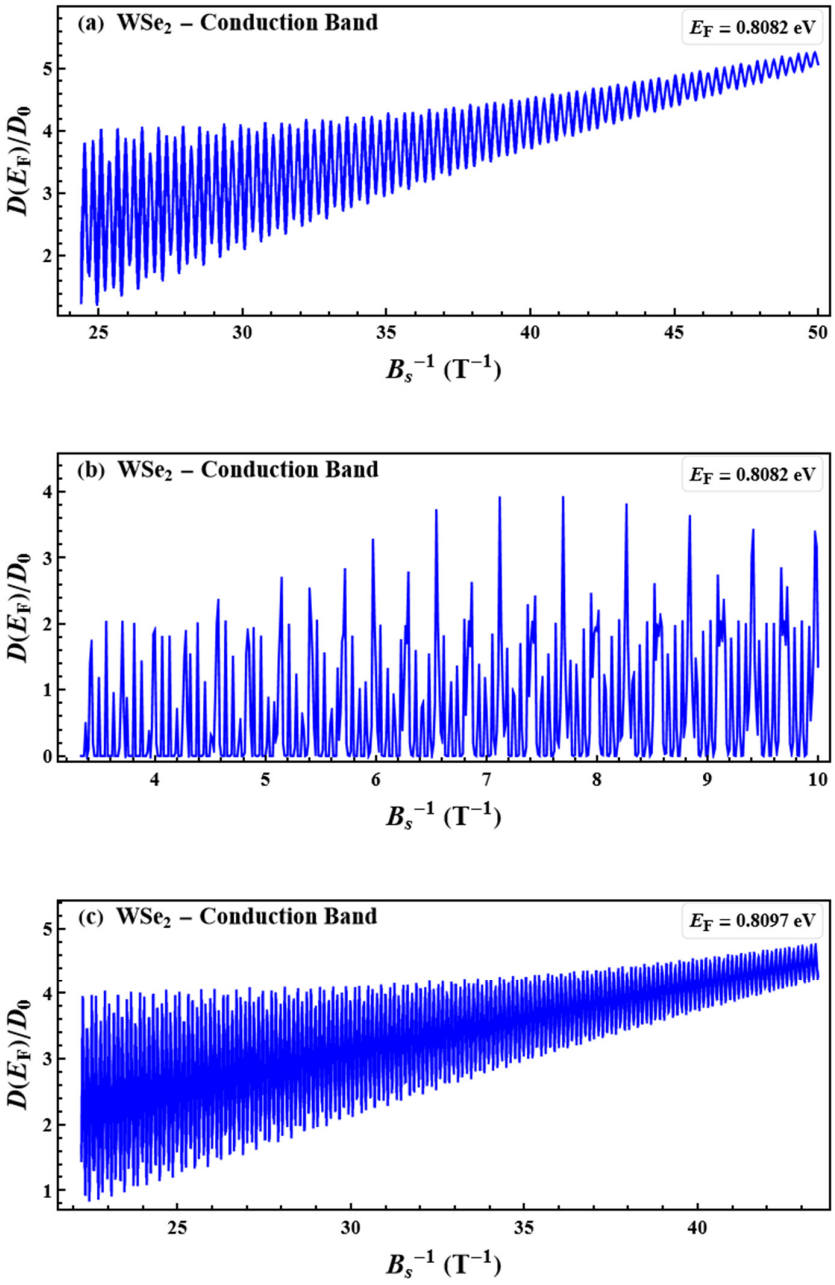


Figure 8. Normalized density of states, $D(E_F)/D_0$, as a function of the inverse of the strain-induced pseudomagnetic field, B_s^{-1}, for monolayer WSe_2. Panels (**a**,**b**) are evaluated at $E_F = 0.8082$ eV over low- and relatively higher-pseudomagnetic-field ranges, respectively, while panel (**c**) is evaluated at $E_F = 0.8097$ eV in the low-field regime. A Gaussian broadening parameter of $\Gamma = 0.003$ meV is used.

The corresponding WSe_2 results exhibit the same PLL-crossing mechanism, although the oscillatory pattern differs quantitatively because of the stronger SOC and the finite conduction-band spin splitting. In the present calculation, the conduction-band SOC parameter is taken as $\lambda_c = 7$ meV, corresponding to a total spin splitting of approximately 14 meV. Panels (a) and (b) are evaluated at $E_F = 0.8082$ eV, whereas panel (c) is calculated at $E_F = 0.8097$ eV. Since these Fermi energies lie slightly above the upper spin-

split conduction-band edge, both spin–valley-resolved conduction branches can contribute to the DOS. In panel (a), the low-field regime contains a dense sequence of closely spaced resonances because many high-index PLLs successively cross the fixed Fermi energy. At higher pseudomagnetic fields, as shown in panel (b), the PLL separation increases and the individual DOS peaks become more clearly resolved. Panel (c) shows that a slight change in the Fermi energy modifies the relative positions of the PLL crossings and produces a more structured modulation of the oscillation amplitude. This behavior results from the superposition of the two spin–valley-resolved PLL sequences and demonstrates the strong sensitivity of the WSe_2 DOS to both the pseudomagnetic field and the selected Fermi energy.

The inverse-field oscillatory behavior predicted here is qualitatively related to quantum-oscillation phenomena observed experimentally in two-dimensional electronic systems under Landau quantization. In monolayer MoS_2, Shubnikov–de Haas oscillations and Landau-level filling have been experimentally resolved [26], demonstrating the characteristic inverse-field periodicity associated with successive level crossings of the Fermi energy. Similar Landau-level spectroscopy has also been reported in WSe_2-based systems [27]. Although these experiments involve real magnetic fields rather than strain-induced pseudomagnetic fields, they provide a qualitative experimental benchmark for the level-crossing mechanism and inverse-field oscillatory structure discussed in Figures 7 and 8.

Figures 9 and 10 present the field dependence of the common conduction-band Fermi energy E_F of monolayer MoS_2 and WSe_2 at fixed electron densities of $n_e = 3 \times 10^{15}\ \mathrm{m}^{-2}$ and $n_e = 6 \times 10^{15}\ \mathrm{m}^{-2}$, respectively. The calculations include both time-reversal-related spin–valley sectors and finite conduction-band SOC, with the Fermi energy obtained self-consistently from the Fermi–Dirac distribution. For both materials, the calculated chemical potential displays oscillatory variations as the strain-induced pseudomagnetic field changes. These features arise because the energies and orbital degeneracies of the PLLs vary with B_s, while the total electron density is held fixed. Successive changes in the occupation of the quantized levels consequently produce a nonmonotonic, approximately sawtooth-like field dependence. The detailed positions and amplitudes of the oscillations differ between MoS_2 and WSe_2 because of their distinct band parameters and conduction-band spin–orbit splittings.

Increasing the electron density from 3×10^{15} to $6 \times 10^{15}\ \mathrm{m}^{-2}$ raises the chemical potential relative to the lowest conduction states and changes the sequence of occupied PLLs. The resulting oscillatory pattern is accordingly reorganized. At the very low temperatures considered here (0.01, 0.1, and 0.5 K), thermal occupation smooths the sharpest filling-related features, most visibly near changes in level occupancy; its extent depends on the local energy-level spacing. Importantly, the numerical convergence analysis confirms that these field-dependent oscillations are insensitive to further increases in the retained number of PLLs. This behavior demonstrates how a strain-induced gauge field can tune the electronic filling response without an externally applied magnetic field.

The oscillatory response in Figures 9 and 10 is consistent with the general filling physics of Landau-quantized 2D electron systems. For example, Alresheedi et al. [28] theoretically reported magnetic-field-dependent chemical-potential oscillations at different carrier densities, including an increase of the mean chemical potential and a rearrangement of oscillatory features with higher density. Experimentally, Gustafsson et al. [27] employed single-electron-transistor spectroscopy to resolve density-dependent Landau-level structure in monolayer WSe_2, while Pisoni et al. [26] observed well-resolved quantum oscillations in n-type monolayer MoS_2. Independent measurements of a GaAs-based 2D electron gas have also demonstrated an oscillating chemical potential whose

structure changes with temperature [29]. These studies establish qualitative connections between Landau quantization, level filling, carrier density, and chemical potential. However, they concern externally applied magnetic fields and, in some cases, significant many-body interactions; the present model instead predicts an analogous filling response produced by a strain-induced pseudomagnetic field. Direct experimental confirmation of the latter Fermi energy oscillations in strained TMD monolayers remains an open challenge.

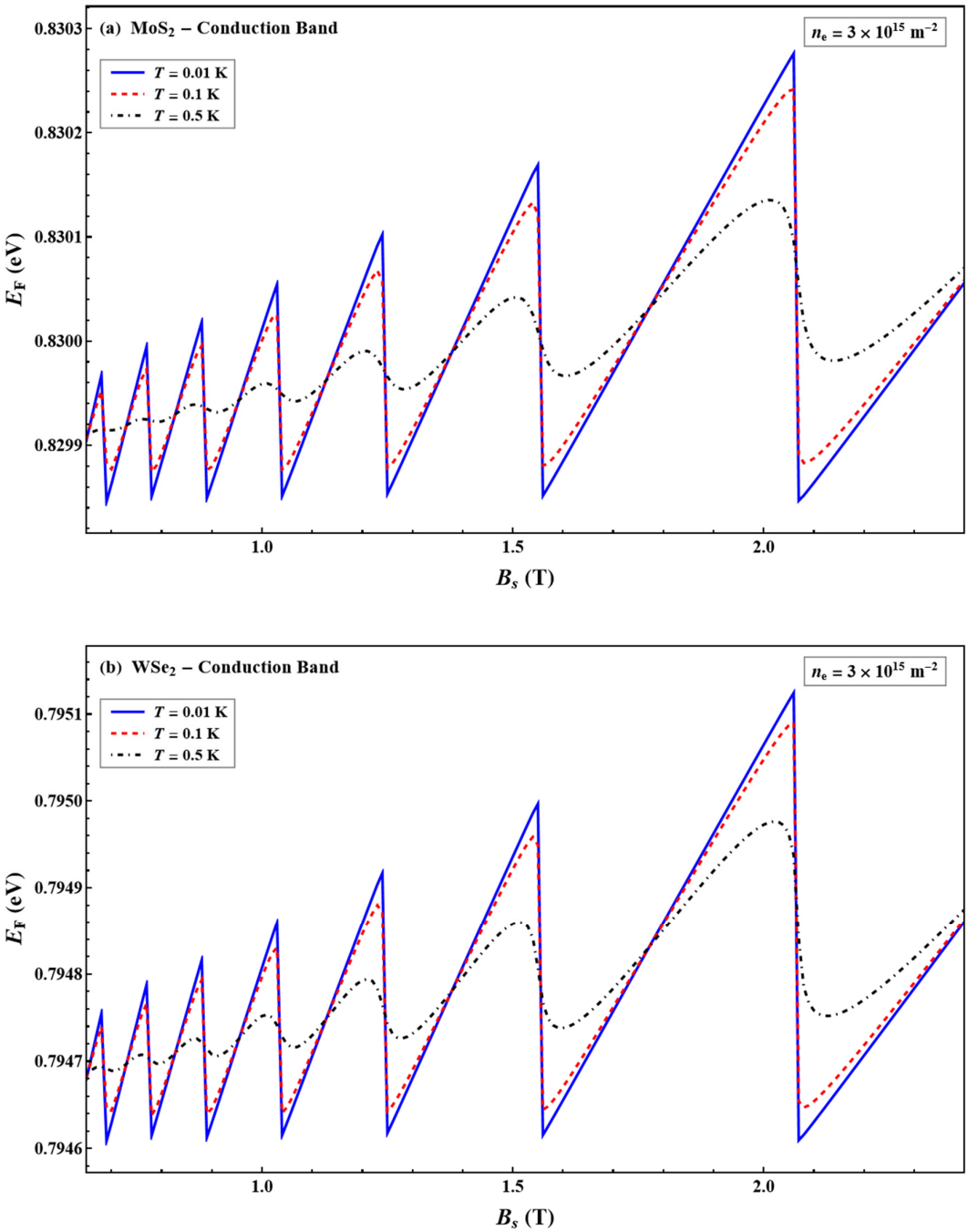


Figure 9. Conduction-band Fermi energy E_F as a function of the strain-induced pseudomagnetic field B_s for monolayer (**a**) MoS_2 and (**b**) WSe_2 at carrier concentrations of $n_e = 3 \times 10^{15}$ m^{-2}. Blue solid, red dashed, and black dot-dashed curves correspond to $T = 0.01$, 0.1, and 0.5 K, respectively.

https://doi.org/10.3390/micro6040096

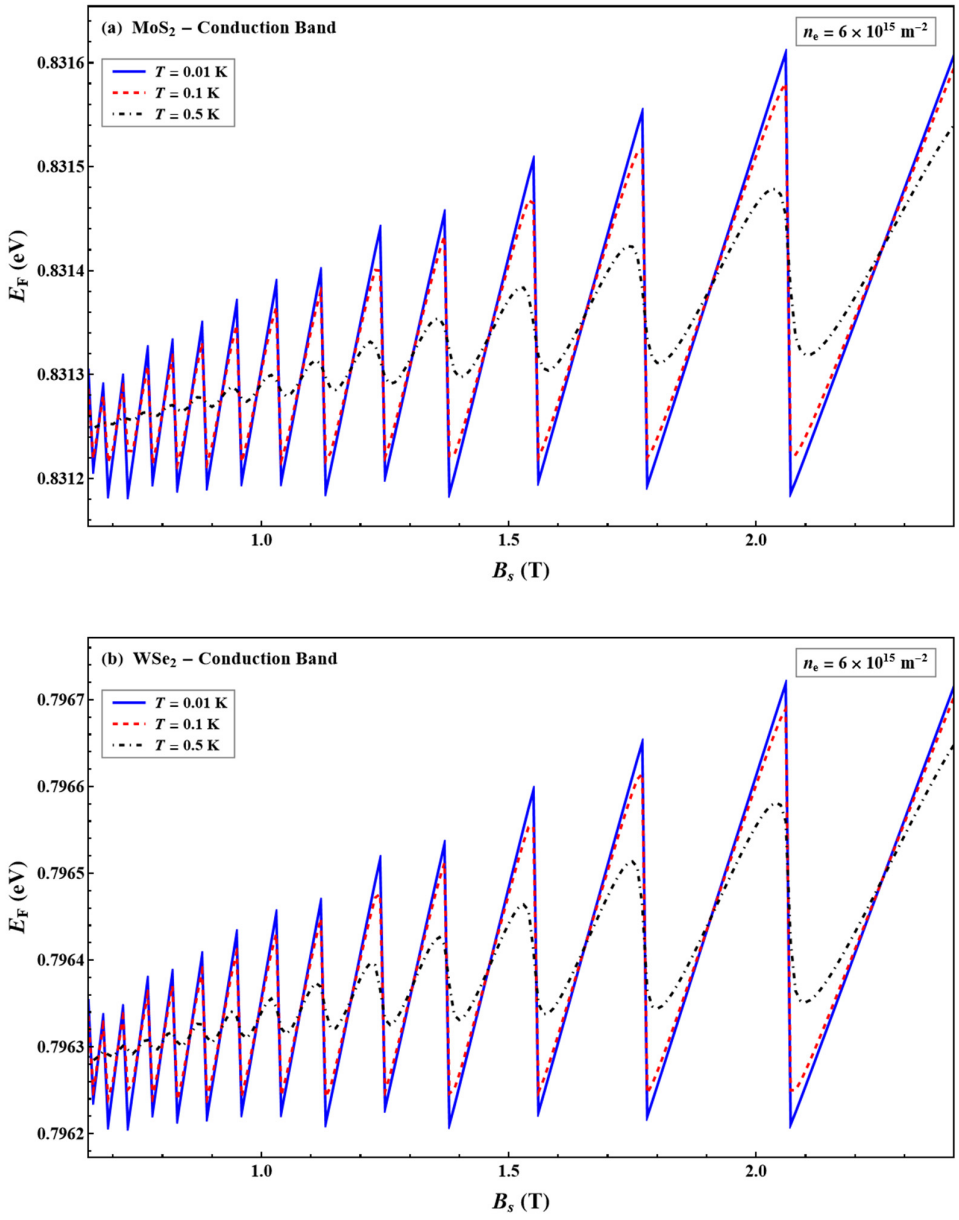


Figure 10. Conduction-band Fermi energy E_F as a function of the strain-induced pseudomagnetic field B_s for monolayer (**a**) MoS_2 and (**b**) WSe_2 at carrier concentrations of $n_e = 6 \times 10^{15}$ m^{-2}. Blue solid, red dashed, and black dot-dashed curves correspond to $T = 0.01$, 0.1, and 0.5 K, respectively.

Having characterized the electronic structure through the DOS and Fermi energy, we next examine the thermodynamic response of the system. We first analyze the thermal average energy as a function of temperature and pseudomagnetic field, followed by the pseudomagnetic susceptibility, which describes the corresponding response to variations in B_s.

Figures 11 and 12 show the temperature dependence of the average energy ⟨E⟩ for monolayer MoS_2 and WSe_2, respectively, at $B_s = 10$, 50, and 80 T. In the conduction band, ⟨E⟩ increases monotonically with temperature for all pseudomagnetic fields because thermal excitation progressively populates higher PLLs. At a fixed temperature, increasing B_s shifts the conduction-band average energy upward, reflecting the larger

quantization energy of the strain-induced PLL spectrum. The valence-band excitation energy also increases with temperature; however, its field ordering is reversed under the adopted edge-referenced definition, with the average excitation becoming smaller as Bs increases. The two spin–valley branches remain close in MoS_2, whereas WSe_2 exhibits a visibly larger branch separation, particularly in the conduction band. This enhanced separation is consistent with the strong SOC in WSe_2 and with the finite conduction-band SOC, $\lambda c = 0.007$ eV. Thus, both materials display the same qualitative thermal behavior, while WSe_2 shows a stronger spin–valley differentiation.

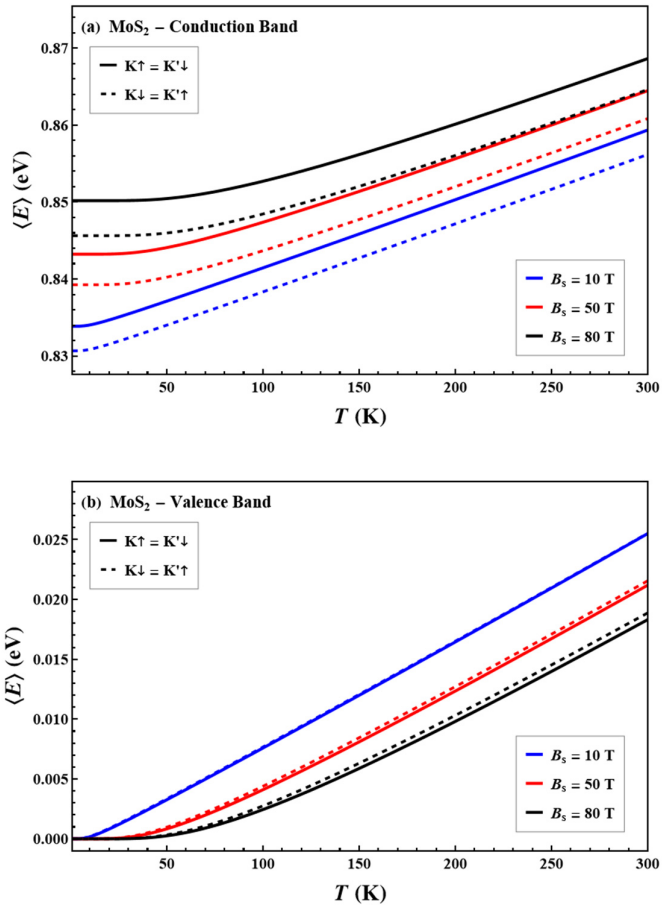


Figure 11. Temperature dependence of the thermal average energy, ⟨E⟩, of monolayer MoS_2 at strain-induced pseudomagnetic fields B_s = 10, 50, and 80 T. Panels (**a**,**b**) show the conduction-band and edge-referenced valence-band results, respectively. Solid and dashed curves correspond to the K↑ = K′↓ and K↓ = K′↑ spin–valley sectors, respectively.

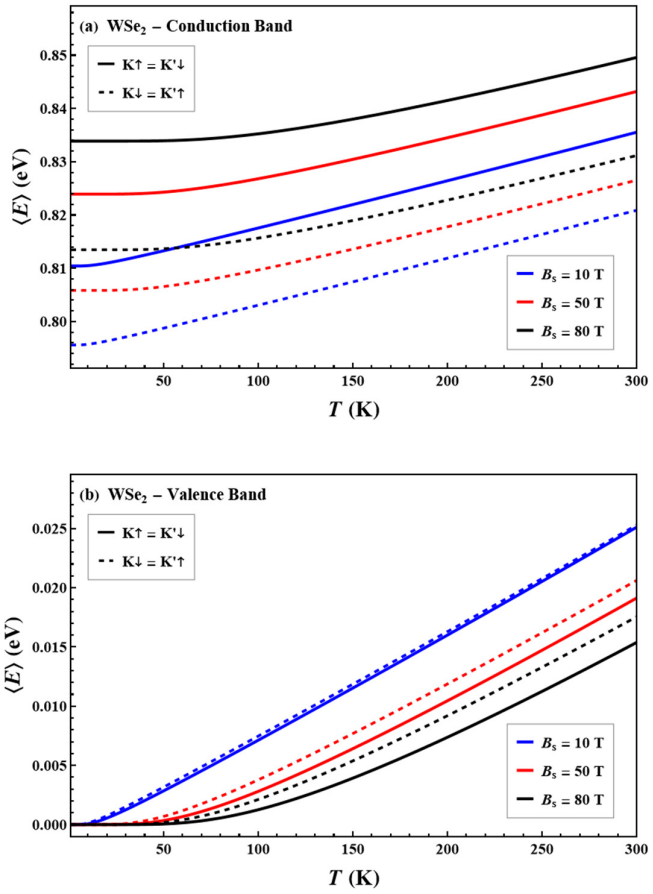


Figure 12. Temperature dependence of the thermal average energy, ⟨E⟩, of monolayer WSe_2 at strain-induced pseudomagnetic fields B_s = 10, 50, and 80 T. Panels (**a**,**b**) show the conduction-band and edge-referenced valence-band results, respectively. Solid and dashed curves correspond to the K↑ = K′↓ and K↓ = K′↑ spin–valley sectors, respectively.

Figures 13 and 14 present the average energy ⟨E⟩ as a function of B_s for MoS_2 and WSe_2, respectively, at T = 100, 200, and 300 K. For both materials, the conduction-band average energy increases smoothly with B_s at every temperature, while increasing the temperature shifts the curves upward because of the enhanced population of higher-energy PLLs. In contrast, the edge-referenced valence-band excitation energy decreases continuously with B_s, although its magnitude increases with temperature. The same overall trends are obtained for MoS_2 and WSe_2, confirming that the pseudomagnetic field controls the quantization scale in both materials. The main quantitative difference is the more pronounced separation between the two spin–valley branches in WSe_2, particularly in the conduction band. This enhanced separation reflects the stronger SOC in WSe_2 together with the inclusion of the finite conduction-band SOC, λ_C = 0.007 eV, which produces a larger differentiation between the two spin–valley-resolved conduction branches.

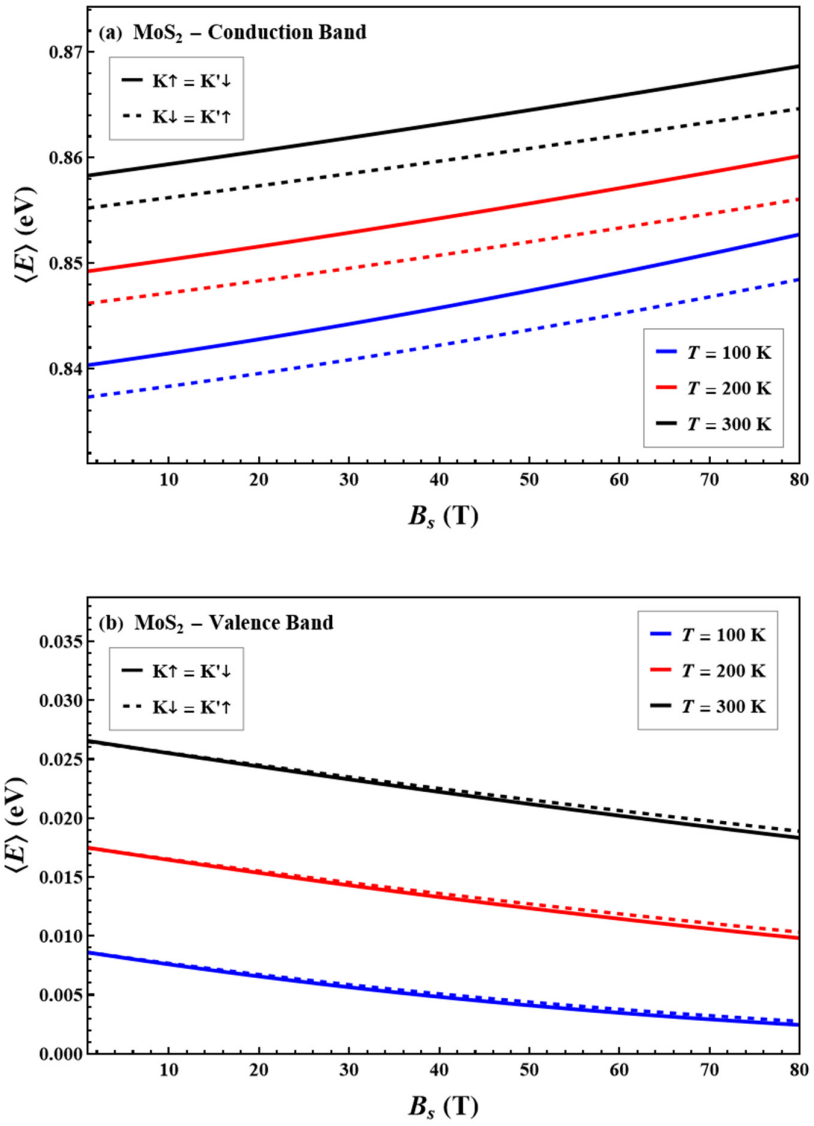


Figure 13. Thermal average energy, ⟨E⟩, as a function of the strain-induced pseudomagnetic field B_s for monolayer MoS_2 at $T = 100$, 200, and 300 K. Panels (**a**,**b**) show the conduction-band and edge-referenced valence-band results, respectively. Solid and dashed curves correspond to the K↑ = K′↓ and K↓ = K′↑ spin–valley sectors, respectively.

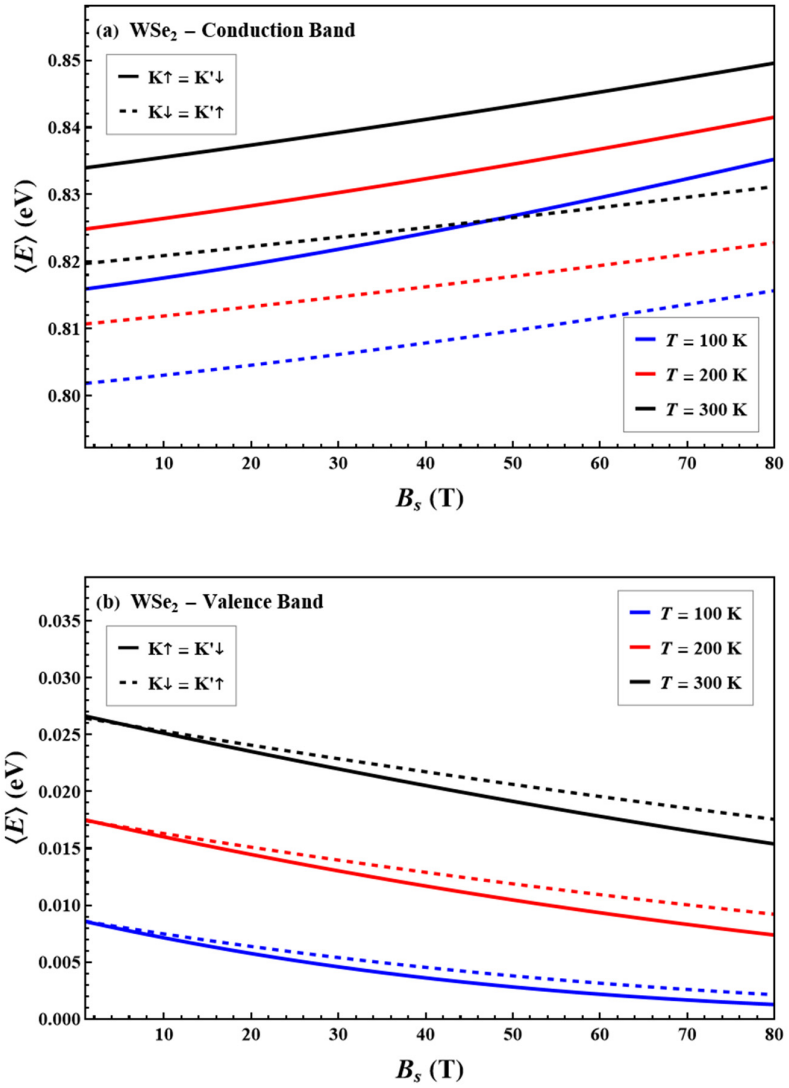


Figure 14. Thermal average energy, ⟨E⟩, as a function of the strain-induced pseudomagnetic field B_s for monolayer WSe_2 at $T = 100, 200,$ and 300 K. Panels (**a**,**b**) show the conduction-band and edge-referenced valence-band results, respectively. Solid and dashed curves correspond to the K↑ = K′↓ and K↓ = K′↑ spin–valley sectors, respectively.

Figures 15 and 16 show the generalized susceptibility, χ_s/μ_B, associated with the strain-induced pseudomagnetic field as a function of B_s for MoS_2 and WSe_2, respectively, over $B_s = 1 - 10$ T at $T = 20, 50,$ and 70 K. In both materials, χ_s/μ_B, remains positive and decreases monotonically with increasing B_s. The response changes most rapidly in the low-field region and progressively weakens at larger fields, where the curves flatten and approach small values. At a fixed B_s, the susceptibility increases with temperature, with the 70 K curve lying above the 50 K and 20 K curves; this thermal separation is strongest at low field and becomes progressively smaller as $B_s$increases. The conduction- and valence-band responses exhibit the same overall field-driven suppression, while the two time-reversal-related sectors K↑ = K′↓ and K↓ = K′↑ remain closely spaced, indicating that spin–valley splitting provides only a small quantitative contribution to the dominant field and temperature dependence.

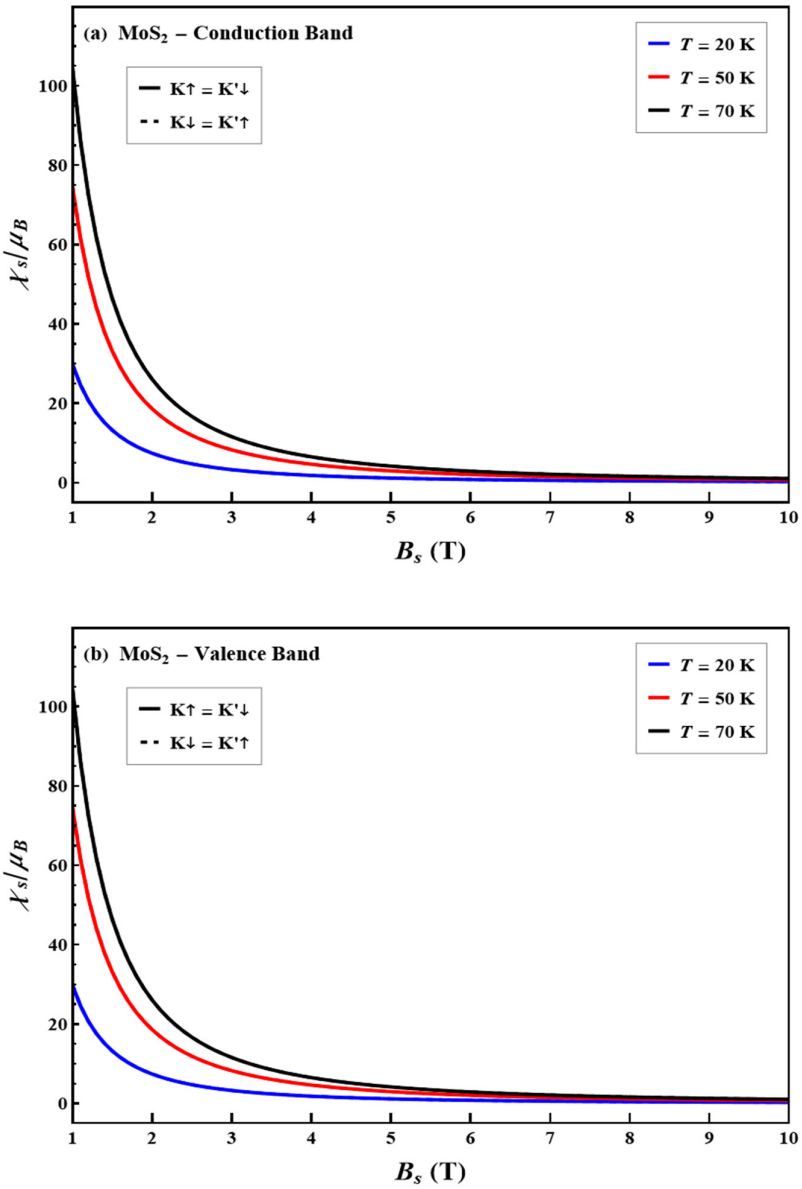


Figure 15. Generalized susceptibility, χ_s/μ_B, as a function of the strain-induced pseudomagnetic field B_s for MoS_2 at T = 20, 50, and 70 K. Panels (**a**,**b**) show the conduction-band and edge-referenced valence-band results, respectively. Solid and dashed curves correspond to the K↑ = K′↓ and K↓ = K′↑ spin–valley sectors, respectively.

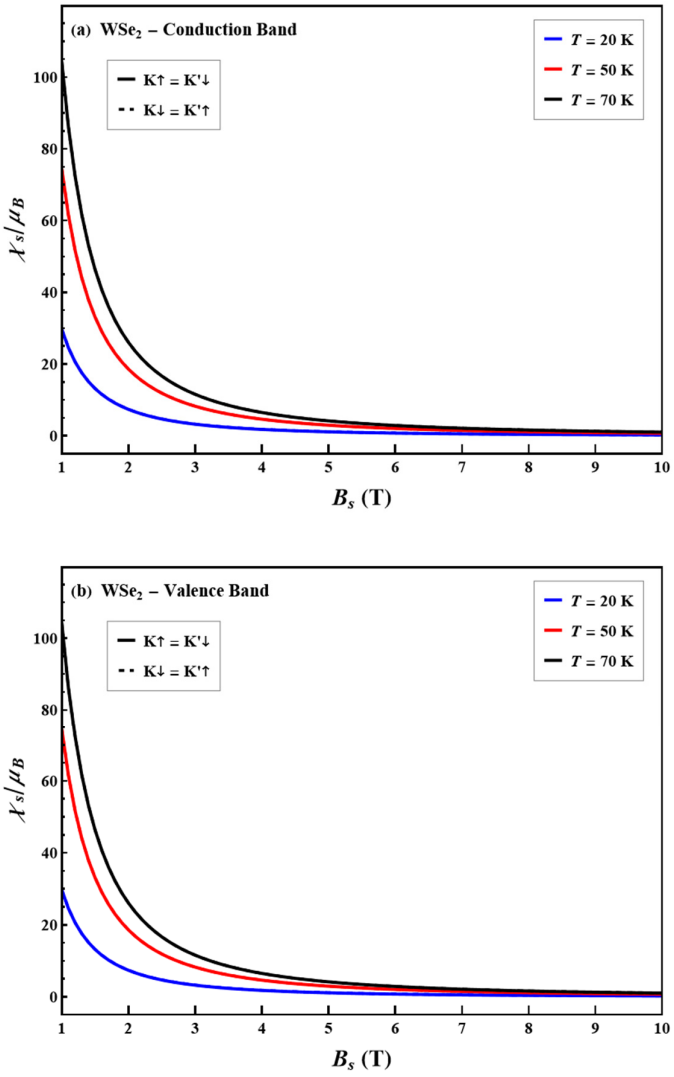


Figure 16. Generalized susceptibility, χ_s/μ_B, as a function of the strain-induced pseudomagnetic field B_s for WSe_2 at T = 20, 50, and 70 K. Panels (**a**,**b**) show the conduction-band and edge-referenced valence-band results, respectively. Solid and dashed curves correspond to the K↑ = K′↓ and K↓ = K′↑ spin–valley sectors, respectively.

4. Conclusions

In conclusion, we investigated the electronic and thermodynamic properties of strained monolayer MoS_2 and WSe_2 within the low-energy massive-Dirac framework in the presence of a strain-induced pseudomagnetic field. Starting from the PLL spectrum, we systematically examined the density of states, the Fermi energy at fixed carrier density, the thermal average energy, and the generalized thermodynamic response to the pseudomagnetic field.

The results show that the strain-induced pseudomagnetic field produces pronounced Landau-like quantization, giving rise to discrete PLLs and characteristic oscillatory behavior in both the DOS and the Fermi energy. The Fermi-energy oscillations are progressively smoothed with increasing temperature as a consequence of thermal broadening, while increasing the carrier density shifts the Fermi level upward and modifies the sequence of PLL crossings. The thermal average energy exhibits a systematic

dependence on both temperature and pseudomagnetic-field strength, reflecting the redistribution of carriers among the quantized levels. The generalized pseudofield susceptibility is most pronounced in the low-field regime and gradually approaches small values as the pseudomagnetic field increases. The spin–valley-resolved calculations further reveal quantitative differences between MoS_2 and WSe_2 arising from their distinct band parameters and SOC strengths, including the finite conduction-band SOC retained for WSe_2.

Building on the strain-induced PLL spectrum, the present work provides a unified picture of how pseudomagnetic quantization governs the electronic and thermodynamic response of monolayer TMDs. Taken together, the calculated observables reveal how strain, temperature, carrier density, and spin–valley coupling collectively shape the response of the quantized electronic system. They also provide complementary, experimentally relevant signatures of strain-induced quantization that may be probed in suitably engineered TMD structures. More broadly, the results demonstrate that strain-generated pseudomagnetic fields offer a versatile route for tuning the electronic, thermal, and spin–valley properties of monolayer TMDs without the need for an externally applied real magnetic field.

Author Contributions: Conceptualization, M.K.E.; Methodology, M.K.E.; Formal Analysis, A.Y.; Investigation, M.K.E.; Data Curation, A.Y.; Writing—Original Draft, A.Y.; Writing—Review and Editing, M.K.E.; Visualization, M.K.E.; Supervision, M.K.E.; Project Administration, M.K.E. All authors have read and agreed to the published version of the manuscript.

Funding: This research received no external funding.

Institutional Review Board Statement: Not applicable.

Informed Consent Statement: Not applicable.

Data Availability Statement: The original contributions presented in this study are included in the article. Further inquiries can be directed to the corresponding author.

Conflicts of Interest: The authors declare no conflicts of interest.

References

1. Novoselov, K.S.; Geim, A.K.; Morozov, S.V.; Jiang, D.; Zhang, Y.; Dubonos, S.V.; Grigorieva, I.V.; Firsov, A.A. Electric Field Effect in Atomically Thin Carbon Films. *Science* **2004**, *306*, 666–669.
2. Wang, Y.; Sarkar, S.; Yan, H.; Chhowalla, M. Critical challenges in the development of electronics based on two-dimensional transition metal dichalcogenides. *Nat. Electron.* **2024**, *7*, 638–645.
3. Torres-Cavanillas, R.; Forment-Aliaga, A. Design of stimuli-responsive transition metal dichalcogenides. *Commun. Chem.* **2024**, *7*, 241.
4. Jo, M.-K.; Lee, E.; Moon, E.; Jang, B.G.; Kim, J.; Dhakal, K.P.; Oh, S.; Cho, S.R.; Hasanah, N.; Yang, S.; et al. Indirect-To-Direct Bandgap Crossover and Room-Temperature Valley Polarization of Multilayer MoS_2 Achieved by Electrochemical Intercalation. *Adv. Mater.* **2024**, *36*, 2407997.
5. Yang, S.; Long, H.; Chen, W.; Sa, B.; Guo, Z.; Zheng, J.; Pei, J.; Zhan, H.; Lu, Y. Valleytronics Meets Straintronics: Valley Fine Structure Engineering of 2D Transition Metal Dichalcogenides. *Adv. Opt. Mater.* **2024**, *12*, 2302900.
6. Xiao, D.; Liu, G.-B.; Feng, W.; Xu, X.; Yao, W. Coupled Spin and Valley Physics in Monolayers of MoS_2 and Other Group-VI Dichalcogenides. *Phys. Rev. Lett.* **2012**, *108*, 196802
7. Peng, Z.; Chen, X.; Fan, Y.; Srolovitz, D.J.; Lei, D. Strain engineering of 2D semiconductors and graphene: From strain fields to band-structure tuning and photonic applications. *Light Sci. Appl.* **2020**, *9*, 190.
8. Sahu, P.; Satpathy, S. Strain theory of the two-dimensional transition metal dichalcogenides. *Phys. Rev. B* **2024**, *109*, 115124.
9. Zhang, Y.; Zhao, H.L.; Huang, S.; Hossain, M.A.; van der Zande, A.M. Enhancing Carrier Mobility in Monolayer MoS_2 Transistors with Process-Induced Strain. *ACS Nano* **2024**, *18*, 12377–12385.

10. Sah, R.K.; Tang, H.; Shahi, C.; Ruzsinszky, A.; Perdew, J.P. Effect of strain on the band gap of monolayer MoS_2. *Phys. Rev. B* **2024**, *110*, 144109.
11. Wang, Y.; Cong, C.; Yang, W.; Shang, J.; Peimyoo, N.; Chen, Y.; Kang, J.; Wang, J.; Huang, W.; Yu, T. Strain-induced direct-indirect bandgap transition and phonon modulation in monolayer WS_2. *Nano Res.* **2015**, *8*, 2562–2572.
12. Rostami, H.; Roldán, R.; Cappelluti, E.; Asgari, R.; Guinea, F. Theory of strain in single-layer transition metal dichalcogenides. *Phys. Rev. B* **2015**, *92*, 195402.
13. Levy, N.; Burke, S.A.; Meaker, K.L.; Panlasigui, M.; Zettl, A.; Guinea, F.; Neto, A.H.C.; Crommie, M.F. Strain-Induced Pseudo-Magnetic Fields Greater Than 300 Tesla in Graphene Nanobubbles. *Science* **2010**, *329*, 544–547.
14. Zhou, H.; Auerbach, N.; Uzan, M.; Zhou, Y.; Banu, N.; Zhi, W.; Huber, M.E.; Watanabe, K.; Taniguchi, T.; Myasoedov, Y.; et al. Imaging quantum oscillations and millitesla pseudomagnetic fields in graphene. *Nature* **2023**, *624*, 275–281.
15. Cheng, Z.; Liu, N.; Deng, J.; Zhang, H.; Pan, Z.; Zhu, C.; Lu, S.; Bai, Y.; Lin, X.; Ji, W.; et al. Twist-angle dependent pseudo-magnetic fields in monolayer $CrCl_2$/graphene heterostructures. *Mater. Horiz.* **2025**, *12*, 473–479.
16. Sahani, D.; Das, S.; Watanabe, K.; Taniguchi, T.; Agarwal, A.; Bid, A. Quantum Transport Spectroscopy of Pseudomagnetic Field in Graphene. *Phys. Rev. Lett.* **2026**, *136*, 166604.
17. Shayeganfar, F. Strain engineering of electronic properties and anomalous valley hall conductivity of transition metal dichalcogenide nanoribbons. *Sci. Rep.* **2022**, *12*, 11285.
18. Kim, S.; Woo, S.; Myoung, N.; Park, H.C. Pseudo-Landau levels on a strain crystal. *J. Korean Phys. Soc.* **2026**, *88*, 1340–1346.
19. Boev, M.V.; Savenko, I.G.; Kovalev, V.M. Impurity-band optical transitions in two-dimensional Dirac materials under strain-induced synthetic magnetic field. *Phys. Rev. B* **2021**, *103*, 245402.
20. Yu, X.; Peng, Z.; Xu, L.; Shi, W.; Li, Z.; Meng, X.; He, X.; Wang, Z.; Duan, S.; Tong, L.; et al. Manipulating 2D Materials through Strain Engineering. *Small* **2024**, *20*, 2402561.
21. Ai, R.; Cui, X.; Li, Y.; Zhuo, X. Local Strain Engineering of Two-Dimensional Transition Metal Dichalcogenides Towards Quantum Emitters. *Nano-Micro Lett.* **2025**, *17*, 104.
22. Kim, B.C.; Kim, Y.; Lee, G.-H. Precision Local Strain Engineering in 2D Semiconductors and Their van der Waals Heterostructures. *Small* **2026**, *22*, e12902.
23. Cazalilla, M.A.; Ochoa, H.; Guinea, F. Quantum Spin Hall Effect in Two-Dimensional Crystals of Transition-Metal Dichalcogenides. *Phys. Rev. Lett.* **2014**, *113*, 077201.
24. Muoi, D.; Hieu, N.N.; Pham, V.T.; Phuc, H.V.; Nguyen, C.V.; Bui, H.D.; Le, P.T.T. Low-energy bands and optical properties of monolayer WS_2. *Optik* **2020**, *209*, 164581.
25. Pető, J.; Dobrik, G.; Kukucska, G.; Vancsó, P.; Koós, A.A.; Koltai, J.; Nemes-Incze, P.; Hwang, C.; Tapasztó, L. Moderate strain induced indirect bandgap and conduction electrons in MoS_2 single layers. *npj 2D Mater. Appl.* **2019**, *3*, 39.
26. Pisoni, R.; Kormányos, A.; Brooks, M.; Lei, Z.; Back, P.; Eich, M.; Overweg, H.; Lee, Y.; Rickhaus, P.; Watanabe, K.; et al. Interactions and Magnetotransport through Spin-Valley Coupled Landau Levels in Monolayer MoS_2. *Phys. Rev. Lett.* **2018**, *121*, 247701.
27. Gustafsson, M.V.; Yankowitz, M.; Forsythe, C.; Rhodes, D.; Watanabe, K.; Taniguchi, T.; Hone, J.; Zhu, X.; Dean, C.R. Ambipolar Landau levels and strong band-selective carrier interactions in monolayer WSe_2. *Nat. Mater.* **2018**, *17*, 411–415.
28. Alresheedi, F. Theoretical calculations to investigate thermodynamic properties of 2D electron gas in InP/InPBiN quantum structure. *Results Phys.* **2023**, *54*, 107042.
29. Nizhankovskii, V.I. Thermodynamics of Two-Dimensional Electron Gas in a Magnetic Field. *Phys. Res. Int.* **2011**, *2011*, 742158.

Disclaimer/Publisher's Note: The statements, opinions and data contained in all publications are solely those of the individual author(s) and contributor(s) and not of MDPI and/or the editor(s). MDPI and/or the editor(s) disclaim responsibility for any injury to people or property resulting from any ideas, methods, instructions or products referred to in the content.